

Particle dynamics of a cartoon dune

To cite this article: Christopher Groh *et al* 2010 *New J. Phys.* **12** 063025

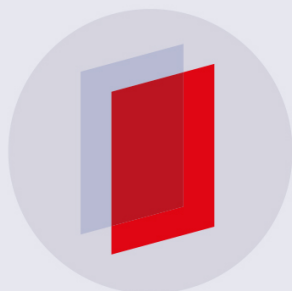
View the [article online](#) for updates and enhancements.

Related content

- [How attractive is a barchan dune?](#)
Christopher Groh, Ingo Rehberg and Christof A Kruehle
- [The physics of wind-blown sand and dust](#)
Jasper F Kok, Eric J R Parteli, Timothy I Michaels *et al.*
- [A two-species continuum model for aeolian sand transport](#)
M Lämmel, D Rings and K Kroy

Recent citations

- [Wet granular matter: a truly complex fluid](#)
Stefanie Strauch and Stephan Herminghaus
- [Observation of density segregation inside migrating dunes](#)
Christopher Groh *et al*



IOP | ebooks™

Bringing you innovative digital publishing with leading voices to create your essential collection of books in STEM research.

Start exploring the collection - download the first chapter of every title for free.

Particle dynamics of a cartoon dune

Christopher Groh^{1,3}, Ingo Rehberg¹ and Christof A Kruelle^{1,2}

¹ Experimentalphysik V, Universität Bayreuth, D-95440 Bayreuth, Germany

² Maschinenbau und Mechatronik, Hochschule Karlsruhe-Technik und
Wirtschaft, D-76133 Karlsruhe, Germany

E-mail: Christopher.Groh@uni-bayreuth.de

New Journal of Physics **12** (2010) 063025 (20pp)

Received 4 November 2009

Published 15 June 2010

Online at <http://www.njp.org/>

doi:10.1088/1367-2630/12/6/063025

Abstract. The spatio-temporal evolution of a downsized model for a desert dune is observed experimentally in a narrow water flow channel. A particle tracking method reveals that the migration speed of the model dune is one order of magnitude smaller than that of individual grains. In particular, the erosion rate consists of comparable contributions from creeping (low-energy) and saltating (high-energy) particles. The saltation flow rate is slightly larger, whereas the number of saltating particles is one order of magnitude lower than that of the creeping ones. The velocity field of the saltating particles is comparable to the velocity field of the driving fluid. It can be observed that the spatial profile of the shear stress reaches its maximum value upstream of the crest, while its minimum lies at the downstream foot of the dune. The particle tracking method reveals that the deposition of entrained particles occurs primarily in the region between these two extrema of the shear stress. Moreover, it is demonstrated that the initial triangular heap evolves to a steady state with constant mass, shape, velocity and packing fraction after one turnover time has elapsed. Within that time the mean distance between particles initially in contact reaches a value of approximately one quarter of the dune basis length.

 Online supplementary data available from stacks.iop.org/NJP/12/063025/mmedia

‘We are right in the open desert,’ said the doctor. ‘Look at that vast reach of sand! What a strange spectacle! What a singular arrangement of nature!’ [1]. In this fictive story of Jules Verne from the 19th century, Dr Samuel Ferguson and his two companions discover the beauty of sand dunes in the deserts of Africa by traveling five weeks in a balloon across the continent. Today, scientists are still overwhelmed by these self-organized granular structures, but they use satellites for observations instead of balloons [2, 3].

³ Author to whom any correspondence should be addressed.

The more descriptive science of the past century [4–6] has changed to a detailed approach in understanding dune dynamics [7]. The crescent-shaped *barchan* dune was chosen as a suitable object because of its relatively fast dynamics. So-called ‘minimal models’ were established to describe the basic dynamics of barchan dunes [8–10]. These two-dimensional (2D) models deal with dune slices along the direction of the driving wind. Briefly, they combine an analytical description of the turbulent shear flow over low elevations [11, 12] with a continuum description, which models the saltation on the surface of the dune [13]. In the next step of complexity, these 2D slices are coupled in the cross-wind direction to model 3D barchan dunes [14]. Laboratory experiments [7, 15–18] and field measurements on Earth [19–21] or satellite observations of Mars [22, 23] reveal the quality of such models. Some aspects of the minimal models have been checked quantitatively in a narrow water flow channel [24–26], and the existence of a shape attractor for barchan dunes [27, 28] has been demonstrated experimentally [29].

Minimal models are continuum models: they deal with the overall shape of the dunes, neglecting the particulate nature of these granular systems. However, the dynamics of dunes is determined by the transport mechanism of the individual grains of sand [4]. Aeolian sand transport consists of two modes of transport: *reptation* in the low-energy regime and *saltation* in the high-energy regime [30]. The saltating grains are carried with the wind and have flight lengths of thousands of grain diameters. The paths of the reptating grains are much shorter. Their motion is initiated by impacts of the saltating grains onto the granular bed [31]. Experiments in wind tunnels with sand traps [32–34] and with particle tracking methods [35–37] give insight into the aeolian grain transport on the level of particle dynamics.

In order to investigate desert dunes under laboratory conditions, it is convenient to use water instead of air [7, 18, 27], since this creates small replicas of aeolian dunes on a much shorter time scale. However, the subaqueous sand transport differs slightly from the aeolian one.

Neglecting the possibility of suspension at high shear velocities, the bed-load transport in water can also be separated into two energy regimes: saltation and surface creep [38–41]. The saltating particles have much shorter flight lengths than in air and, in contrast to the reptating particles, the creeping particles are directly dragged by the fluid and always stay in contact with the bed surface. Particle tracking experiments in flow channels with denser fluids than air, like water or silicon oil, have been performed to investigate the erosion, transport and deposition of grains of sand on a granular bed [42–46].

The particle dynamics at the surface transfers itself into the bed. The packing density of the granular bed decreases from the inner layers towards the outer fluidized layer, which has a thickness of a few grain diameters in a laminar flow [45]. The observation of segregation effects indicates that the sediment in the sand bed is mixed during the process of sand transport and associated ripple formation [47]. Besides global granular transport, the transition between creeping and saltating particles is also a matter of interest [32, 41–43, 48].

The research presented here addresses three questions: (i) How does the fluid transport the particles? (ii) How is particle transport related to overall dune motion? (iii) How is fluid flow influenced by the presence of the dune? For this purpose we created an experimental realization of a minimal dune model—a cartoon dune. It is a migrating isolated heap on a plane surface reminiscent of a barchan dune in the desert. Our experiment reveals the details of particle transport above, on and inside this solitary dune, together with the driving water flow field. For direct access to the particles, our dune is designed with a thickness of less than two particle diameters and is, therefore, quasi-2D.

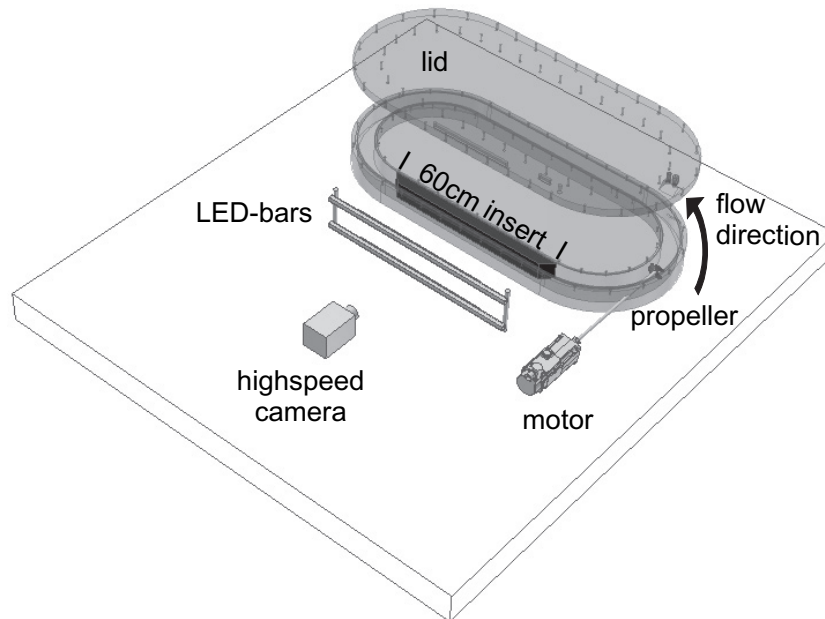


Figure 1. Sketch of the experimental setup.

A sketch of our experimental setup is shown in figure 1. The main part consists of a closed flow channel machined from perspex. The height of the channel amounts to $H = 60$ mm and its width is 50 mm. The length of the straight section is 600 mm, and the curves have an outer diameter of 500 mm and an inner diameter of 400 mm. The channel is filled with distilled water. The flow is generated by a propeller with a diameter of 45 mm, which is installed in the curve following the section of measurements. The propeller is driven by a motor with a shaft that is placed in the middle of the channel profile. The flow direction is counter-clockwise viewed from above. We narrow the section of measurements to create quasi-2D conditions, comparable to a Hele-Shaw [49] cell. For that purpose we use a black plastic insert, which constricts the channel to a width $W = 3$ mm. This leads to an aspect ratio of $H/W = 20$.

For the calculation of Reynolds number Re in the 3 mm wide gap, we measure the flow velocity \vec{u} with an ultrasonic Doppler velocimeter (UDV) manufactured by Signal Processing SA. This device measures the vertical velocity profiles $\vec{u}(y)$. From these profiles we extract the mean horizontal velocity u_{mean} by averaging along the central 80% of the profiles. The kinematic viscosity of water at experimental temperature (20.5 ± 0.3 °C) is $\nu \approx 1$ mm² s⁻¹. The flow velocity is kept at $u_{\text{mean}} = 0.65$ m s⁻¹, which corresponds to $Re = u_{\text{mean}}H/\nu = 39\,000$. Instead of natural sand we use spherical white glass beads (SiLibeads), which have a radius of $r = 1.00 \pm 0.01$ mm and a density of $\rho = 2.51$ g cm⁻³. For the model dune, the overall mass of the beads amounts to $m = 6.5$ g, which corresponds to 629 particles.

To characterize the particle transport in our experiment, we investigate the threshold of incipient motion for the glass beads. Therefore, we prepare a flat granular bed and determine the shear velocity

$$u^* = \sqrt{\nu \left. \frac{du_x}{dy} \right|_{\text{surface}}}$$

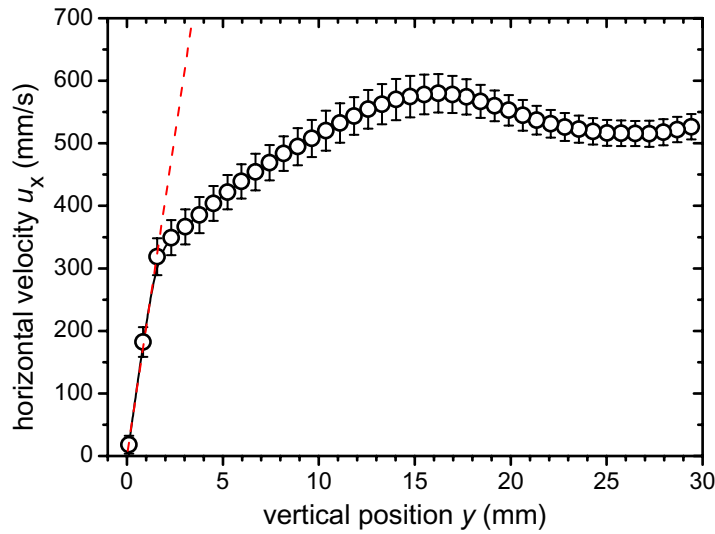


Figure 2. Velocity profile $u_x(y)$ of water flow at the threshold of incipient motion. The dashed red line is a linear fit to the three lowest data points, yielding the shear velocity u^* .

near the surface. The corresponding profile $u_x(y)$ and the slope within the laminar boundary layer are shown in figure 2. We observed that particle motion sets in at the critical shear velocity $u_c^* = 14 \text{ mm s}^{-1}$. This number is used for the calculation of the critical particle Reynolds number

$$Re_c = \frac{u_c^* 2r}{\nu}$$

and the critical Shields parameter

$$\Theta_c = \frac{u_c^{*2}}{g(s-1)2r},$$

with the acceleration of gravity $g = 9.81 \text{ m s}^{-2}$, the density of water $\rho_f = 1 \text{ g cm}^{-3}$ and the specific density $s = \rho/\rho_f$. The resulting $Re_c = 28$ is about six times larger than the typical value for aeolian dunes $Re_{c,\text{air}} = 5$, whereas $\Theta_c = 0.007$ is comparable to its aeolian counterpart $\Theta_{c,\text{air}} = 0.010$ [29].

The model dune is observed with a high-speed camera (IDT, MotionScope M3), which is placed in front of the straight part of the channel. The camera is set to a resolution of 1280×256 pixels at $2000 \text{ frames s}^{-1}$. For a sufficiently bright illumination we use two bars of light-emitting diodes (LED-bars), as shown in figure 1. They lighten the section of measurements from below and above to obtain a homogeneous brightness.

The experimental procedure is as follows. After the flow tube is filled with distilled water, a funnel with a 3 mm long slit is used to pour glass beads into the channel. The experiment starts with the triangular heap shown in figure 3 at $t = 0 \text{ s}$. The five subsequent snapshots show the temporal evolution of the initial triangular heap towards an asymmetric heap moving downstream. After $t = 3 \text{ s}$ the heap reaches the characteristic steady-state shape known from central slices of barchan dunes along their migration direction [19]. In the images the glass beads appear as bright discs in front of the dark background. For their localization we use the circle

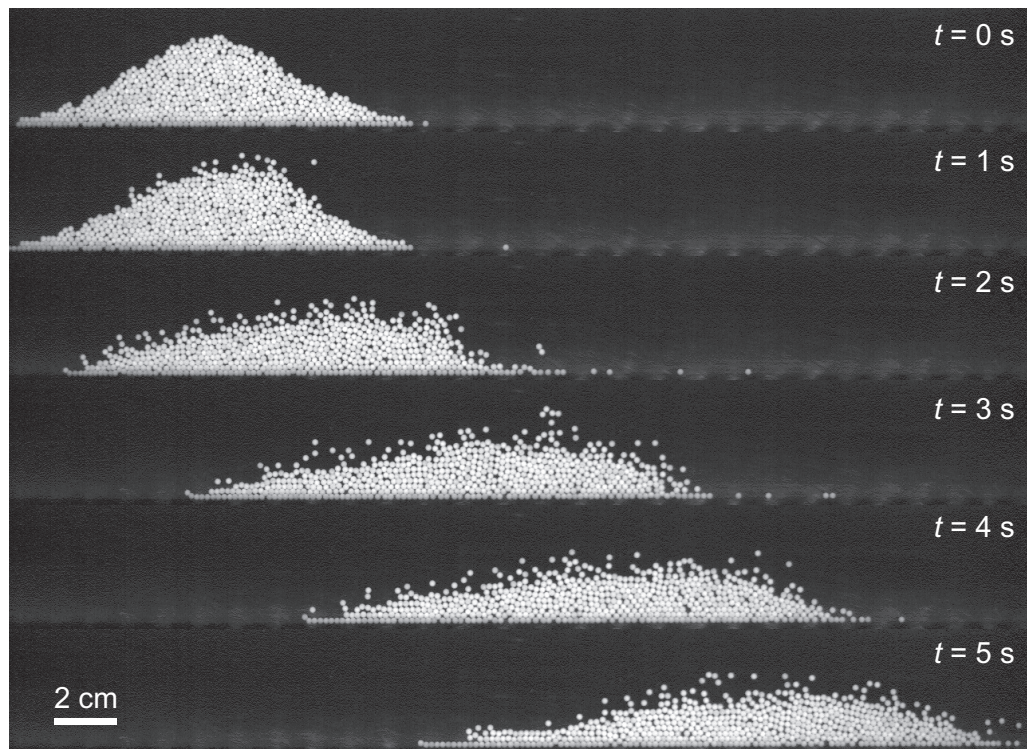


Figure 3. Six time sequenced snapshots showing side views of a developing barchan dune slice composed of white glass beads.

Hough transformation as described in detail in [50, 51]. With this image-processing technique all bead positions in every recorded frame are found. The high-speed camera allows particle tracking for each individual grain, which makes it possible to study the particle dynamics of dunes and the mixing process within dunes.

To visualize the mixing we present figure 4. At the beginning, all detected beads of the data set are colored with a continuous color gradient from the left to the right, as the snapshot at $t = 0$ s shows. As time evolves, the traceable beads retain their initial color, and the non-traceable ones are painted black. As the flow sets in, the grains at the surface of the upstream side are carried away and fall onto the downstream side, where they roll further downwards. In nature this side is called the slipface. From the color code, it can be seen that the inner beads rest in place. The first cycle of mixing is passed after $t = 5$ s, when again most of the blue circles are at the windward side.

For a quantitative measure of the mixing process, we investigate the temporal evolution of the distances $d_{i,j}$ between those particles i and j which are initially in contact. Six representative histograms are plotted in figure 5. The initially sharp distribution broadens with time, and after $t = 5$ s the distribution spans the complete basis dune length l_{dune} . This basis length is determined by the bulk part of the dune as defined later (see figure 12(a)) and turns out to be $l_{\text{dune}} = 190$ mm. The growth of the mean distance $d = \langle d_{i,j} \rangle$ and its standard deviation are shown in the inset of figure 5. This indicates that, within the first turnover time t_{turnover} of about 5 s, the mean distance between particles initially in contact reaches a value of approximately one quarter of the dune basis length.

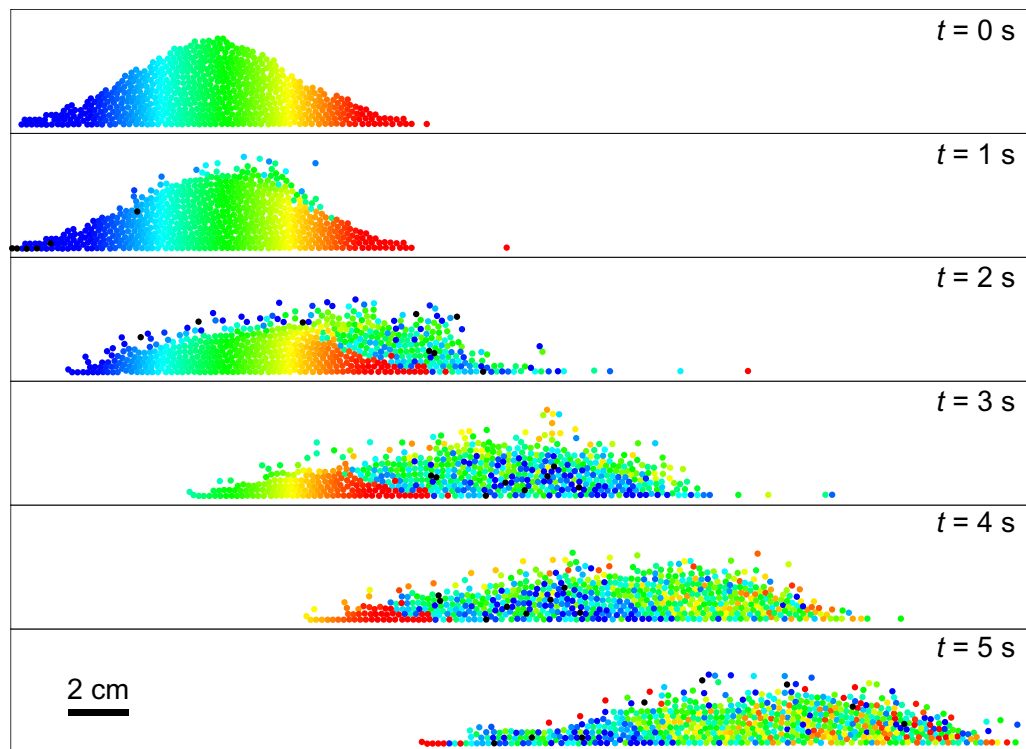


Figure 4. The particles detected in figure 3 are drawn as discs and color coded with respect to their horizontal positions at $t = 0$ s (see animated movie 1, available from stacks.iop.org/NJP/12/063025/mmedia).

Moreover, once all particle positions are known, other quantities describing the dynamics of the dune can be extracted. As shown in figure 6(a), the number of glass beads N is slightly fluctuating within 1%. This is primarily due to particles flowing in and out of the frame, and is partly caused by detecting failures. Although only particles from the surface are in motion, the center of mass of the dune migrates downstream with a velocity v_{com} . From the positions of all beads in the frame, both the center of mass and its velocity are determined. It can be seen in figure 6(b) that v_{com} takes a constant value after $t = 2$ s. This coincides with the relaxation towards the steady-state shape, which is demonstrated by the constant height of the center of mass h_{com} in figure 6(c).

Alternatively, the relaxation process can be characterized by measuring the area packing fraction φ_a within the core of the dune, which is composed of inner static particles. For this purpose we calculate the Voronoi tessellation of each frame [52]. The packing fraction is obtained as the ratio between the cross-sectional area of a spherical glass bead and the corresponding area of its Voronoi cell. In order to characterize only the core beads, we exclude those beads with $\varphi_a < 2/3 \varphi_{\text{max}}$. The maximal packing fraction φ_{max} can be larger than one, because an overlap of particles is possible in the 2D projection of a 3D packing. In our narrow channel of thickness $3r$, the maximal packing fraction $\varphi_{\text{max}} = \pi/3$ is obtained by assuming a 2D square lattice with a lattice constant of $2\sqrt{3}r$. The crystal basis consists of two beads in contact forming an angle of 30° with respect to the plane of this lattice.

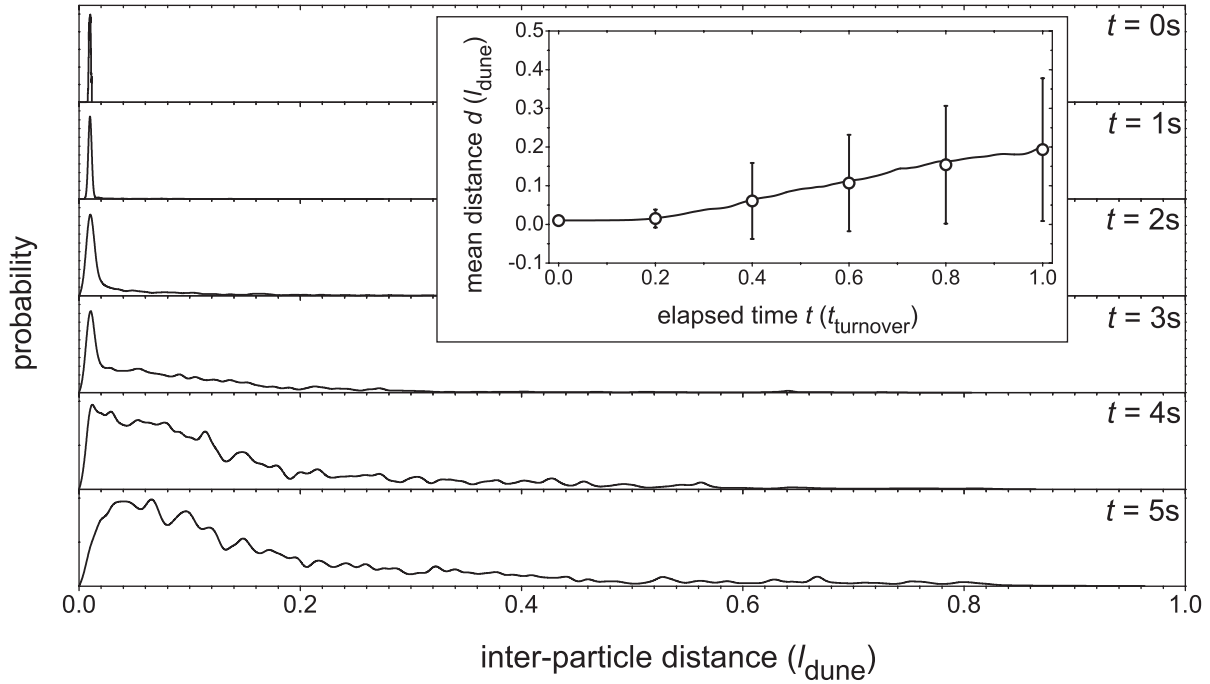


Figure 5. Six histograms corresponding to figure 4 showing the temporal evolution of the distribution of distances $d_{i,j}$. The probability distributions are individually scaled with respect to their maxima. The inset shows the temporal evolution of the mean distance d . The six data points correspond to the histograms, and their standard deviations are represented by the error bars.

In figure 7 the resulting Voronoi cells of the six snapshots of figure 3 are overlaid to all detected beads drawn as gray discs. The cells are color coded with respect to their area. The loss of the blue cells indicates that the packing fraction decreases during the time of measurements. This is quantitatively demonstrated by figure 6(d), where the temporal evolution of the spatial mean packing fraction φ_{mean} corresponding to these Voronoi cells is plotted. In addition to the relaxation of v_{com} and h_{com} , φ_{mean} also takes a constant value after $t = 3$ s.

The investigation of the transient demonstrates that the initial triangular heap evolves to a steady state with constant mass, shape, velocity and packing fraction after about one turnover time t_{turnover} has elapsed. Within that time the mean distance between particles initially in contact reaches a value of approximately one quarter of the dune length l_{dune} .

The presented Voronoi method has the advantage of revealing the temporal evolution of the packing fraction, but it has the disadvantage of being operational only within a small fraction near the core of the dune. In order to obtain meaningful results also in the surrounding area of the dune, we obtain the local area packing fraction from the possibility for each pixel to be shaded by a particle during a certain time. The relation between φ_a and the volume packing fraction φ_v is

$$\varphi_v = \frac{4N\pi r^3}{3AW} = \frac{4r}{3W}\varphi_a,$$

where N is the number of particles in a certain area A . In our geometry $r/W = 1/3$ and thus $\varphi_v = 4/9 \varphi_a$. This yields for the maximum value $4/9 \times \pi/3 \approx 0.47$.

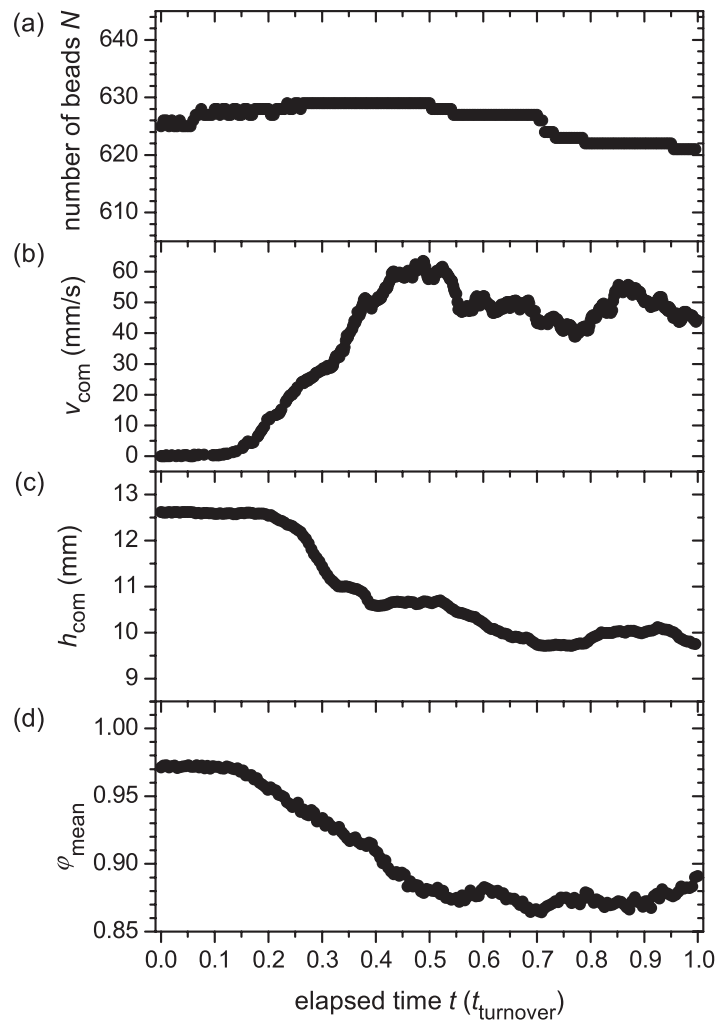


Figure 6. Time evolution of (a) the number of beads N , (b) the velocity of the center of mass of the dune v_{com} , (c) the height of the center of mass h_{com} and (d) the temporal evolution of the mean packing fraction φ_{mean} obtained from the Voronoi method. Every 50th data point is plotted.

The experimentally obtained field $\varphi_v(x, y)$ is shown in figure 8. Here, the time average is taken over 1 s, which corresponds to 2000 single frames. For technical reasons the frames are shifted according to the center of mass of the dunes.

The mean velocity field of the particles is calculated similar to $\varphi_v(x, y)$. Its absolute value $v(x, y)$, its x -component $v_x(x, y)$ and its y -component $v_y(x, y)$ are plotted in figure 8. The field $v(x, y)$ shows that the velocity increases with increasing height above the dune surface. This indicates that the grain movement changes from creeping to saltation—i.e. freely swimming in the water stream. This behavior is also reflected by $v_x(x, y)$. Notably, $v_x(x, y)$ has almost no negative values, indicating that the recirculation bubble at the downstream side [53] is not strong enough to push the sinking beads backwards. The field $v_y(x, y)$ visualizes the erosion and deposition process: at the upstream side the particles are lifted and above the slipface they rapidly fall.

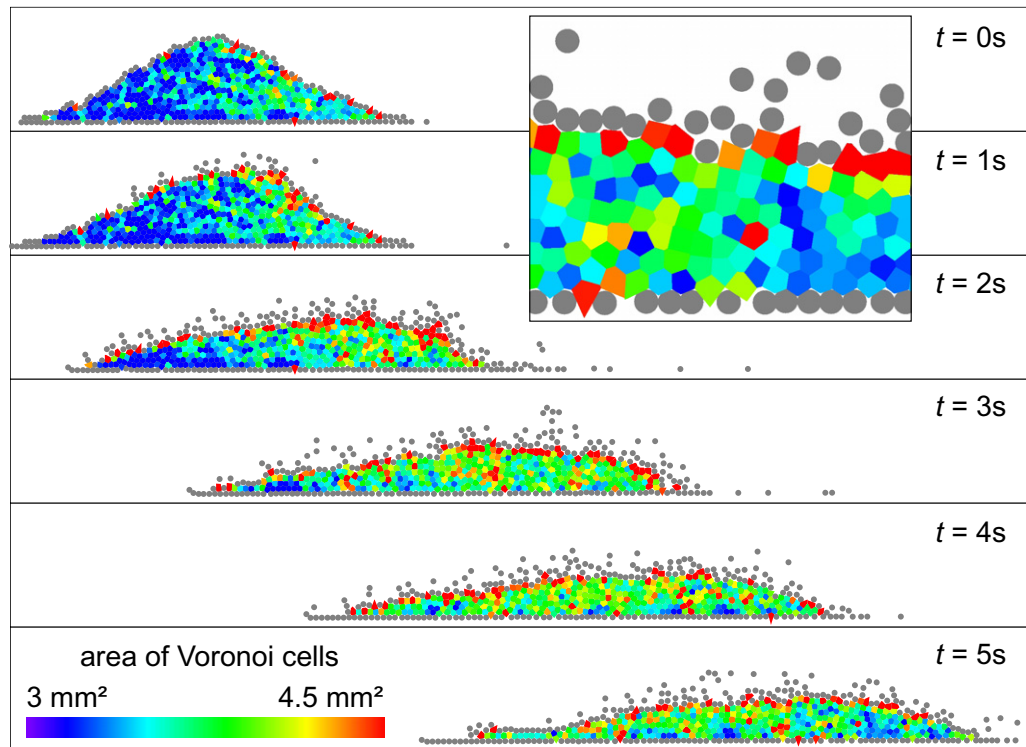


Figure 7. The particles detected in figure 3 are drawn as gray discs. Overlaid are the Voronoi cells of the inner particles, color coded with respect to their size. The inset shows a detail of the snapshot at $t = 5$ s.

The motion of the individual particles results from the interplay with the driving water flow. To illuminate this interaction we need the velocity field of the water flow, which can be measured with the UDV. However, the UDV needs a couple of seconds to acquire a single velocity profile. This is too long for recording the velocity field within the time the dune needs to propagate along the section of measurements. We overcome this problem by measuring the flow field around a steady dune made of plastic instead of the moving dune. The contour of this dummy is obtained from the snapshot at $t = 4$ s in figure 3 by drawing a smoothed envelope around the densely packed bulk of the dune. The result is shown as a red line in figure 9(a). The dummy is decorated with glass beads to simulate the surface roughness, which determines the size of the laminar boundary layer.

We define five characteristic areas (A–E), as shown in figure 9(a), to compare the vertical velocity profiles of the grains and the water flow in figure 9(b). The vertical grain velocity profiles $v_x(y)$ are extracted from $v_x(x, y)$ by averaging horizontally in the corresponding areas. The vertical water velocity profiles $u_x(y)$ are recorded by crossing two ultrasonic beams above the dune surface to get an averaged data set within each area.

The highest measured velocities are found near the crest of the dune. For the water flow this is a manifestation of the incompressibility condition in our closed channel. It is notable that in the areas A–D the particle velocity is finite at such positions y where the water velocity is zero. This can be explained by the fact that the flow velocities are measured with the plastic dummy, which fails to take into account the motion of the particles on the surface. In area E, the water

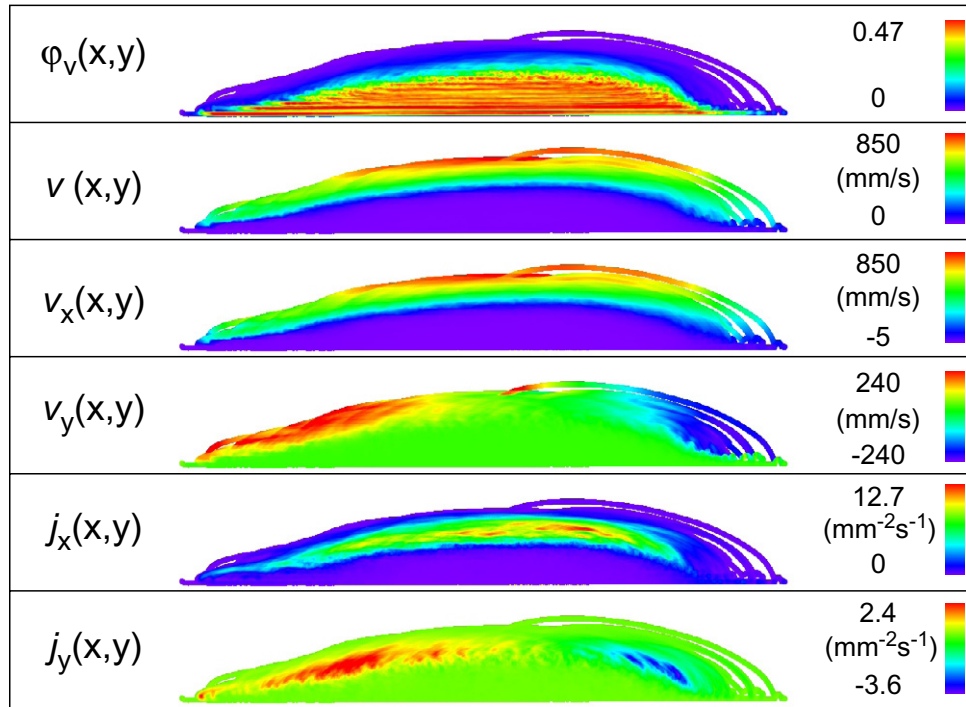


Figure 8. Time-averaged fields of the measurement shown in figure 3 between $t = 4$ s and 5 s. The width corresponds to 33.7 cm in the experiment, and the height of each panel to 4.1 cm. The numbers on the right-hand side of each panel correspond to the minimal and maximal value of the color code.

flow velocity changes its sign at lower heights, which is an indication of the recirculation bubble. In contrast, the grain motion does not follow the water flow in the wake of the dune. In all areas, the velocity gradients of the water profiles are steeper than the ones of the beads. This might result from the fact that the particles cannot follow the water flow immediately due to inertia. Notably, the maximal velocities of both, water and beads, amount to 850 mm s^{-1} , which is more than one order of magnitude larger than the migration velocity of the dune, $v_{\text{com}} \approx 50 \text{ mm s}^{-1}$, measured as the center-of-mass motion. This reflects the mass ratio between the dune and its active surface layer, which has a thickness of about one particle diameter.

From the velocity gradient of the water flow near the surface of the dune (see figure 2), we calculate the shear stress of the water flow as

$$\tau = \eta \left. \frac{du_x}{dy} \right|_{\text{surface}},$$

assuming $\eta = 10^{-3} \text{ Pa s}$ for water at 20°C . Here, the additional turbulent shear stress is neglected, because near fixed walls in the area of the viscous boundary layer the eddy viscosity goes to zero [54]. The resulting values for τ , as shown in figure 10, quantify the slope of the water profiles near the surface of the dune and give a measure of the local drag force. The shear stress increases along the upstream side of the dune and reaches a maximum value before the crest. Above the slipface, τ decreases and even reverses sign in the region of the recirculation bubble and relaxes further downstream. This qualitative behavior corresponds to the analytical description of the wind shear stress used in the theoretical model by Kroy *et al* [9, 10].

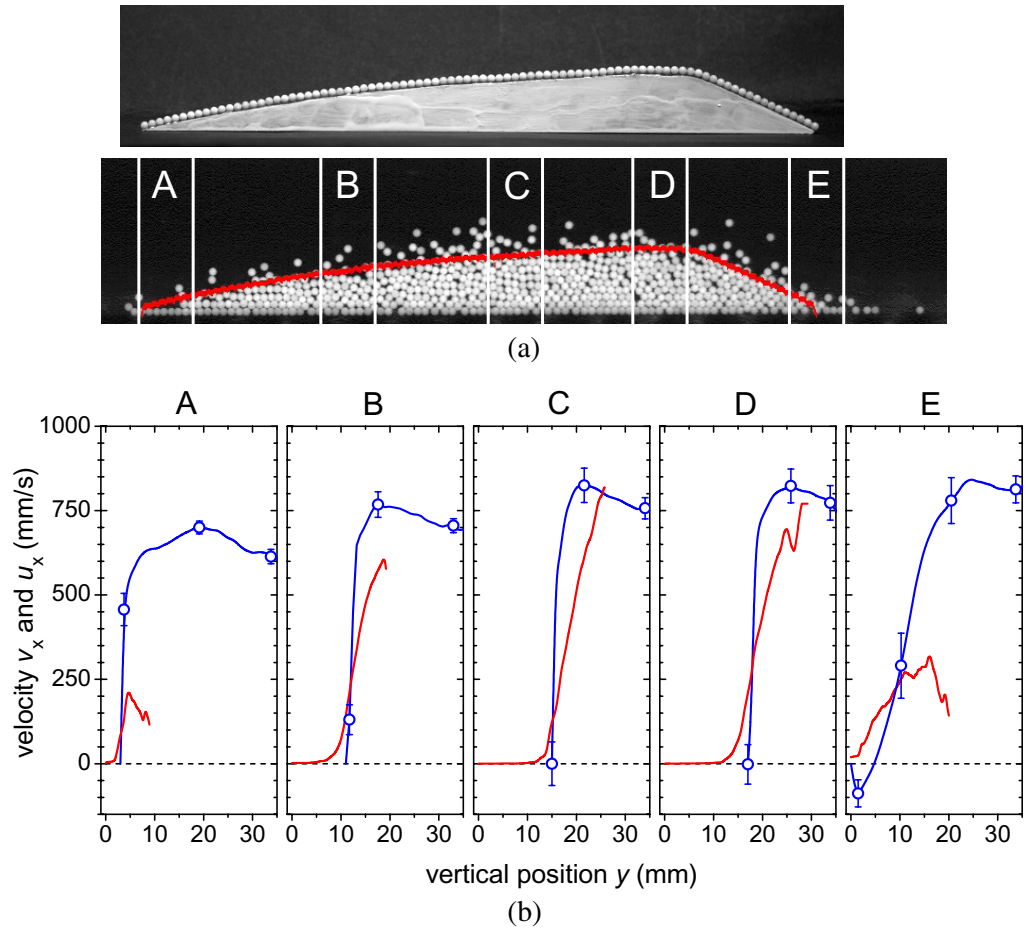


Figure 9. Panel (a) shows the plastic dummy decorated with glass beads and a detail of the snapshot at $t = 4$ s in figure 3. The red line indicates the profile of the plastic dummy used for the determination of the water flow field. The five areas tagged with white lines and capitals correspond to panel (b), which provides the comparison between the vertical velocity profiles $v_x(y)$ of grains (red lines) and $u_x(y)$ of water flow (blue lines) in the selected areas. Each profile consists of 100 measured data points, of which a few representatives are plotted with error bars.

The resulting particle fluxes $j_x(x, y)$ and $j_y(x, y)$ are shown in figure 8. They are the product of the particle density $\varphi_v(x, y)/V_{\text{bead}}$ times $v_x(x, y)$ or $v_y(x, y)$, respectively, where $V_{\text{bead}} = 4\pi/3 \text{ mm}^3$ is the volume of a glass bead. In analogy to figure 9(a), we extract the averaged vertical flux profiles of the horizontal flux $j_x(y)$ as presented in figure 11(a). From these profiles the particle flow rates as a function of the vertical position

$$I_x(y) = \int_0^W \int_0^y j_x(y') dy' dz$$

are extracted by integrating $j_x(y)$ with the vertical position y and the width W of the flow channel. The resulting curves are plotted in figure 11(b).

To specify the nature of the particle transport, we distinguish between beads that have contacts to other beads forming the bulk shown as the gray shaded area in figure 12(a), and

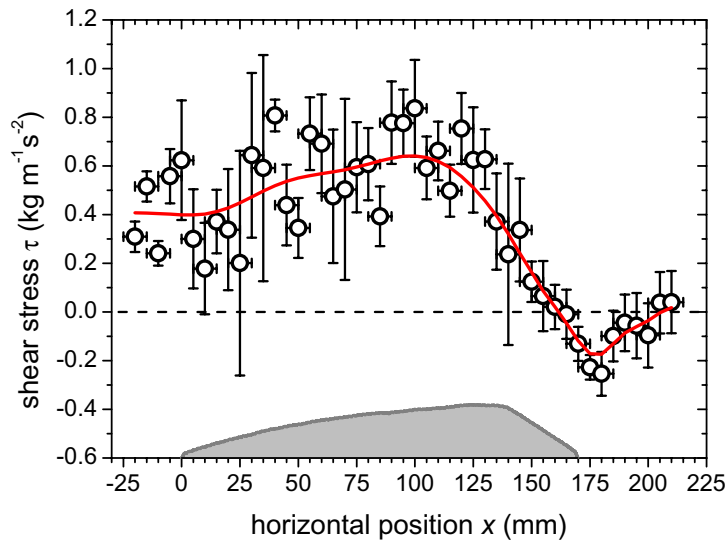


Figure 10. Shear stress of water flow at the dune surface. A smoothing of the data points yields the red line, which is supposed to guide the eye. The gray shaded area symbolizes the location and shape of the plastic dummy.

beads that move freely in the water stream without contact with the bulk. The contact criterion is fulfilled when the centers of two beads fall within a distance shorter than $2.1r$. The beads within the bulk are composed of resting beads and creeping beads, but only the creeping beads contribute to the flux density. The motion of the free flying particles above the surface is named saltation. It can be seen that, at every position along the dune, the average vertical positions of creeping particles are near the surface $h(x)$ and the average vertical positions of saltating particles are located two to three particle diameters above. The vertical positions are determined as the first moment of the vertical particle flux distributions. The distributions are calculated with a spatial running average along the dune with a fixed width of 13 mm corresponding to the areas in figure 8.

We define the values of the spatially averaged integral particle flow rate $I_{x,\text{creep}} = I_x(y = H)$ for creeping particles. $I_{x,\text{salt}}$ for saltating particles is defined likewise. The total particle flow rate results as $I_{x,\text{total}} = I_{x,\text{creep}} + I_{x,\text{salt}}$. All three flow rates are shown as a function of the horizontal position in figure 12(b). The spatial profiles of the separated flow rates show that saltating beads contribute a larger part of the dune motion than creeping beads. Both flow rates reach their maximum values near the crest of the dune, as is known from natural dunes in the desert [13, 55].

The overall erosion rate

$$q = \frac{d^2 N}{dt dx}$$

can be obtained as the spatial derivative of the total flow rate $dI_{x,\text{total}}/dx$. The erosion rate, as shown in figure 12(c), matches qualitatively with the local slope of the dune surface dh/dx . If $q > 0$, the beads are entrained into the water stream and will strengthen the total flow rate. If $q < 0$, the beads are deposited on the surface of the dune and the value of $I_{x,\text{total}}$ will decrease. Along the upstream side, q is greater than zero and becomes negative behind the crest with a

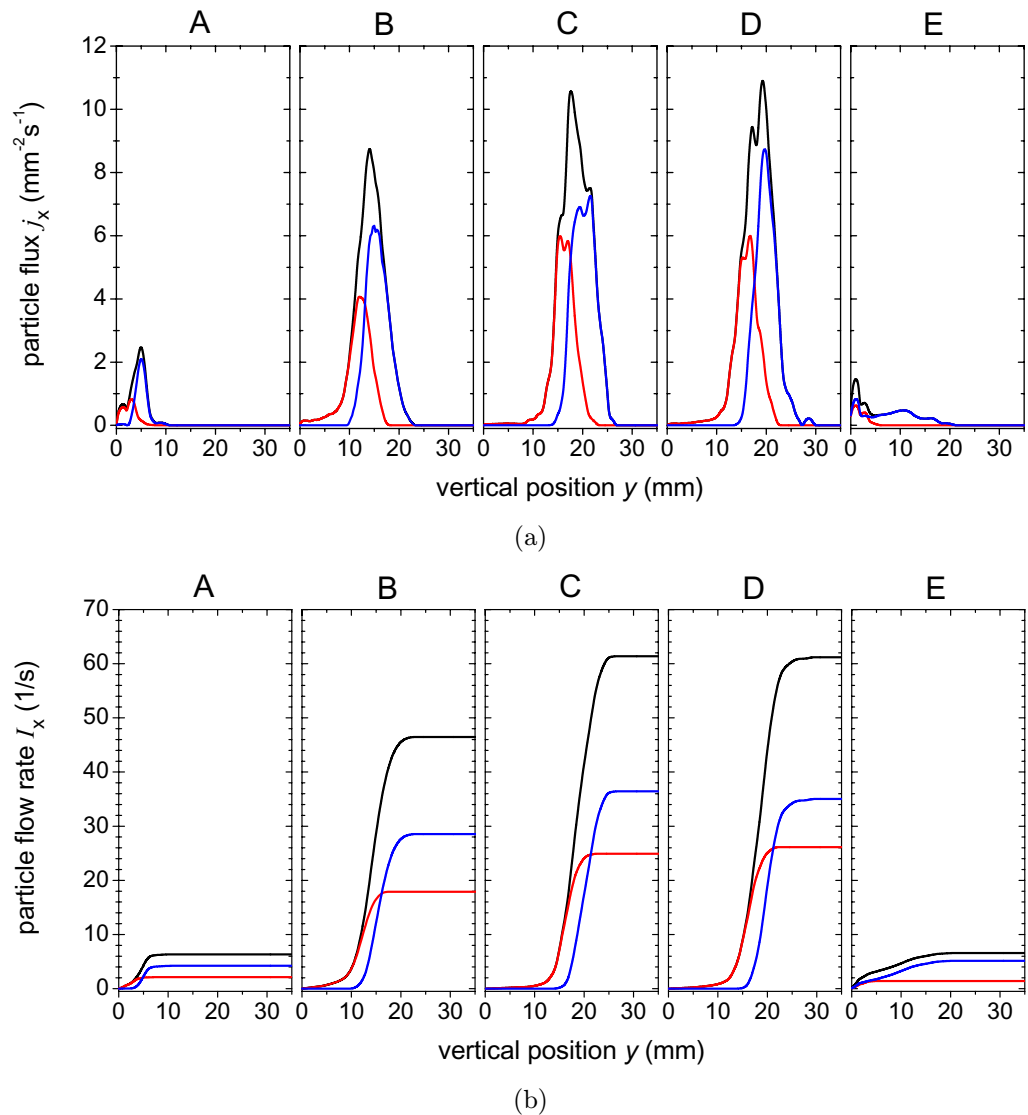


Figure 11. Panel (a) shows the particle flux $j_x(y)$ and panel (b) shows the particle flow rate $I_x(y)$ for all beads (black lines), beads with contacts (red lines) and freely moving beads (blue lines). The data sets are obtained from the corresponding five areas in figure 9(a).

maximal deposition onto the slipface. The plateau near the crest indicates a constant flow rate. These observations correspond to the color code of $j_y(x, y)$ in figure 8. Notably, the position of the maximal deposition matches with the position of the maximal negative shear stress in figure 10.

The erosion and deposition of sand leads to a temporal change in the height of the dune surface. In the steady state the dune moves shape invariantly, and consequently the relation between the changing sand flow rate and the deformation of the dune shape becomes constant. From the conservation of mass, a term for the migration velocity of dunes (v_{com} in our experiment) can be derived as [4, 55]

$$v_{\text{com}} \sim \frac{dI_{x,\text{total}}}{dh} = \text{const.}$$

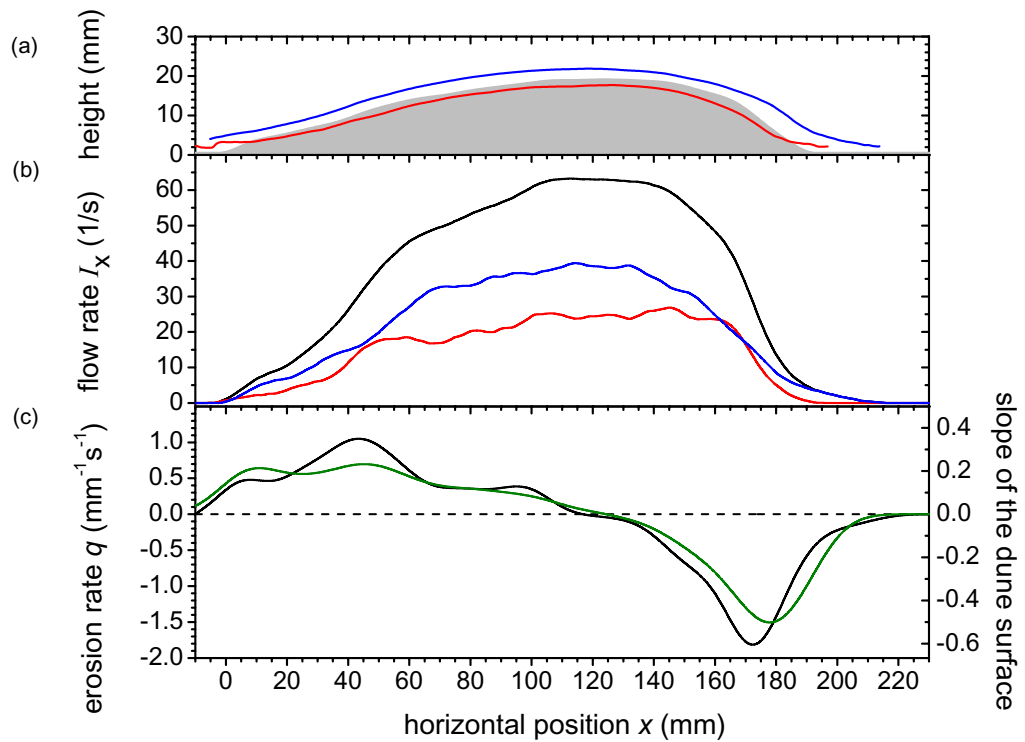


Figure 12. (a) Spatial profiles of the averaged vertical positions of creeping (red) and saltating (blue) particles. The gray shaded area symbolizes the bulk of the dune. (b) Spatial profiles of flow rates $I_{x,creep}$ for creeping (red) and $I_{x,salt}$ for saltating (blue) particles. The black line indicates the sum $I_{x,total}$ of both types. (c) Spatial profile of the local erosion rate q (black line) and the local slope of the dune surface (green line).

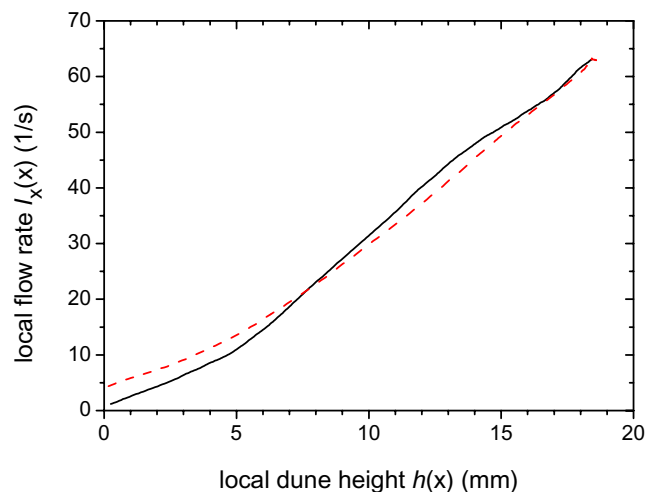


Figure 13. Local relation between total flow rate $I_{x,total}(x)$ and height of the dune $h(x)$ for the upstream side (black solid line) and the downstream side (red dashed line).

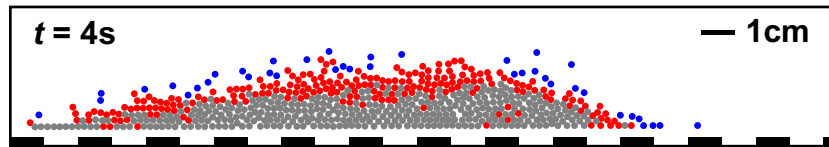


Figure 14. The figure shows a detail of the snapshot at $t = 4$ s in figure 3. The detected particles are drawn as discs and color coded with respect to their type: resting particles (gray), creeping particles (red) and saltating particles (blue). See animated movie 2 (available from stacks.iop.org/NJP/12/063025/mmedia) for the corresponding image sequence between $t = 4$ and 5 s.

In field measurements, this simple formula is used to check the present steady state of a desert dune [55]. For our model dune, the relation of sand flow rate $I_{x,\text{total}}(x)$ and dune height $h(x)$ at a certain horizontal position x is plotted in figure 13. The dune is partitioned at the crest into an upstream side and a downstream side. Above a height of about 4 mm (two grain diameters), the slope $dI_{x,\text{total}}/dh$ becomes constant for both sides, additional confirmation for the steady state.

As mentioned above, the bulk of the dune is composed of resting particles and creeping particles. To separate them, we use the threshold velocity $v_{\text{th}} = 5 \text{ mm s}^{-1}$ as criteria. The value of v_{th} is given by the standard deviation of the velocity distribution of all beads. Note that $v_{\text{th}} \approx 1/10v_{\text{com}}$. It can be seen in figure 14 that sometimes beads in the core of the dune are set in motion, which results from the regrouping of beads due to the erosion and deposition processes. Moreover, the snapshot in figure 14 illustrates that only a few particles are completely detached from the surface. This corresponds to $\varphi_v(x, y)$, shown in figure 8.

These observations are quantitatively shown in figure 15(a), with the distributions of the particle densities n_r (resting), n_c (creeping) and n_s (saltating). For the analysis, every recorded image is divided into columns with a width of 1 cm. The particle densities are determined as the time-averaged number of particles counted in each column between $t = 4$ and 5 s. For technical reasons the frames are shifted according to the center of mass of the dune.

The distributions of n_r and n_c in figure 15(a) show an excess of creeping particles on the downstream side, where the deposition occurs. At the upstream bottom of the dune, n_c and n_s increase. They take constant values in the middle section and decrease in the deposition area. Note that the local densities n_c and n_s show that there are more creeping particles than saltating particles, but figure 12(b) shows that the flow rate of the saltating beads contributes the larger part of $I_{x,\text{total}}(x)$. This can be explained by the higher speed of the saltating particles.

The particle tracking method (see figure 4) allows for the investigation of transitions between the three types of beads in our experiment. Because every transition has two directions, we have to distinguish between rest–creep, creep–rest, creep–saltation, saltation–creep, rest–saltation and saltation–rest. The number of transitions per second gives the transition rate. To simplify the notation, we label each connected pair with one variable: T_{rc} (rest and creep), T_{cs} (creep and saltation) and T_{rs} (rest and saltation). The local distributions of the transition rates corresponding to figure 15(a) are shown in figures 15(b)–(d). In the areas of erosion and deposition, T_{rc} takes a local maximum. The maximum of T_{cs} lies at the crest. The high values of all transition rates indicate the frequent collisions between beads during dune migration.

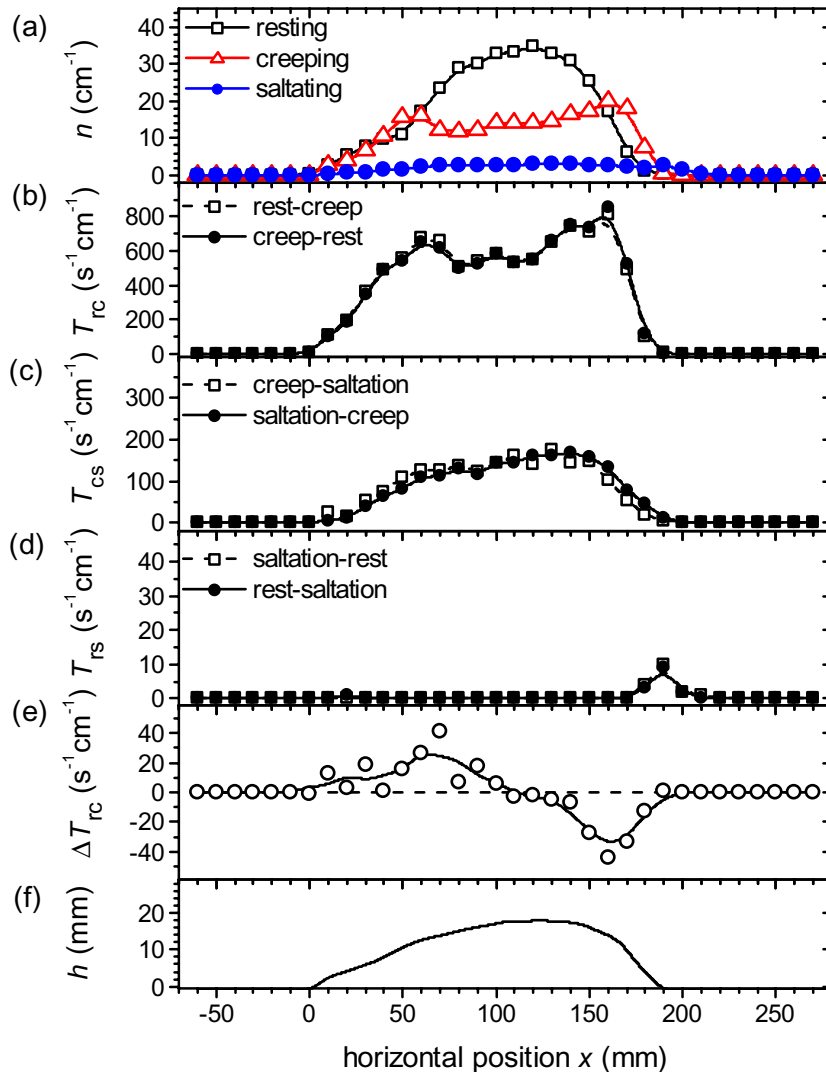


Figure 15. Local particle densities for resting (n_r), creeping (n_c) and saltating (n_s) particles are plotted in (a). Panels (b)–(d) show the pairs of transition rates T_{rc} , T_{cs} and T_{rs} between the three types of particles. The difference between the rest–creep and creep–rest transition in (b) gives ΔT_{rc} in panel (e). The contour of the dune bulk h is shown in panel (f).

While in aeolian sand transport, resting particles are lifted by the impact of other grains [30, 31], the distribution of T_{rs} in figure 15(d) shows that the saltating beads do not originate from resting beads, but from creeping beads dragged by the fluid along the surface. The peak at the downstream side results from single beads, which are temporally not connected to the bulk of the dune. The net rate of erosion and deposition is obtained by subtracting the two parts of T_{rc} , which yields ΔT_{rc} in figure 15(e). The resulting curve fits to the erosion rate shown in figure 12(c). The distribution of n_r in panel (a) reflects the contour of the bulk, shown in figure 15(f).

To conclude, we designed an experiment that allows the direct measurement of the particle dynamics and the surrounding driving water flow above and inside a 2D barchan dune model.

The measurement of the particle dynamics inside the dune reveals the nature of the crawling motion of dunes, whose speed is one order of magnitude smaller than that of the creep and saltation of individual grains. This ratio is, of course, not universal but specific for our downsized model dune. Due to the possibility of distinguishing between creeping and saltating particles, we show that the erosion rate consists of comparable contributions from both. The saltation flow rate is slightly larger, whereas the number of saltating particles is one order of magnitude lower than that of the creeping ones. The velocity field of the saltating particles is comparable to the velocity field of the driving fluid, although that of the particles lags behind.

Moreover, it is demonstrated that the initial triangular heap evolves to a steady state with constant mass, shape, velocity and packing fraction after one turnover time has elapsed. Within that time the mean distance between particles initially in contact reaches a value of approximately one quarter of the dune basis length, a number that serves to quantify the mixing process.

The shear stress of the water flow is shown to be related to the particle erosion rate, as well as the slope of the dune surface. It can be observed that the spatial profile of the shear stress reaches its maximum value upstream of the crest, while its minimum lies at the downstream foot of the dune. The particle tracking method reveals that the deposition of entrained particles occurs primarily in the region between these two extrema of the shear stress. Due to this deposition, most of the mass of the dune is preserved. The upstream shift of the shear stress has been a crucial element for explaining the steady state in minimal models.

In summary, our experimental findings justify the assumptions of the minimal models, namely (i) the time-scale separation, (ii) the separation of the dune in a fluidized layer and an immobile inner part, and (iii) the reduction of the flow field to the shear stress acting on the surface.

Time-scale separation means that the migration of the cartoon dune, i.e. the change in its shape, occurs on a time-scale one order of magnitude slower than the temporal changes in the particle transport and the fluid field. For desert dunes the separation of the time scales is more pronounced because of their larger size in comparison to the grain size. Due to this time-scale separation the models can be simplified by using stationary solutions for the particle transport and the fluid field.

Our experiment reveals that the dune is separated in a fluidized surface layer and an immobile inner part. The minimal models use a continuum description for sand flux within the fluidized layer. Consequently, they neglect individual particles and only take dune shape into account. The disadvantage is that this method reduces the complex motion of particles to a single sand flux equation including some empirical parameters, without giving any information about the individual fate of particles, which would be important for understanding the mixing properties of the dune.

The shear stress acting on the surface is a measure of the interaction between the fluid and the particles. For the continuum description of particle transport, the shear stress is calculated analytically. For this purpose the turbulent eddies at the lee side are ignored and replaced by a heuristic separation bubble. However, our experiment shows that a more complex physics takes place on the lee side of the dune, where the particles are trapped by recirculating flows. This feature should be included in a more refined model.

Since our cartoon dune shows that the particle dynamics of dunes can be modeled with less than a thousand particles, it seems to be possible to treat the interaction between individual particles and the fluid in more detail. In order to do this, only the moving particles

of the fluidized layer must be taken into account. The bulk of resting inner particles could be ignored.

The presented experimental results are difficult to measure in the desert. One might track micrometer-size probes during several years of dune migration and simultaneously monitor the wind field in detail. This will be a tedious job, because of the long time scales and the lack of control of the environmental parameters.

In general, agitated granular matter is known to show segregation whenever particles differ in size or density. The dynamics of this ubiquitous phenomenon could not be studied so far in the field. By using a bidisperse mixture of particles or particles of different density, our tracking method promises new insights, which can finally accompany existing dating methods for dunes. Thus, the laboratory setup serves as a kind of time lapse camera for geological processes spanning eons in nature.

Acknowledgments

It is a pleasure to thank Kai Huang and Matthias Schröter for stimulating suggestions. We are grateful for support from Deutsche Forschungsgemeinschaft through Kr1877/3-1 (Forschergruppe 608 ‘Nichtlineare Dynamik komplexer Kontinua’).

References

- [1] Verne J 1863 *Cinq Semaines en Ballon* (Paris: J. Hetzel & Cie)
- [2] Andreotti B, Fourrière A, Ould-Kaddour F, Murray B and Claudin P 2009 Giant aeolian dune size determined by the average depth of the atmospheric boundary layer *Nature* **457** 1120–3
- [3] Flowing barchan sand dunes on Mars, <http://antwrp.gsfc.nasa.gov/apod/ap090420.html>
- [4] Bagnold R A 1941 *The Physics of Blown Sand and Desert Dunes* (London: Chapman and Hall)
- [5] Pye K and Tsoar H 1990 *Aeolian Sand and Sand Dunes* (London: Unwin Hyman)
- [6] Lancaster N 1995 *Geomorphology of Desert Dunes* (London: Routledge)
- [7] Andreotti B, Claudin P and Douady S 2002 Selection of dune shapes and velocities part 1: dynamics of sand, wind and barchans *Eur. Phys. J. B* **28** 321–39
- [8] Andreotti B, Claudin P and Douady S 2002 Selection of dune shapes and velocities, part 2: a two-dimensional modelling *Eur. Phys. J. B* **28** 341–52
- [9] Kroy K, Sauermann G and Herrmann H J 2002 Minimal model for sand dunes *Phys. Rev. Lett.* **88** 054301
- [10] Kroy K, Sauermann G and Herrmann H J 2002 Minimal model for aeolian sand dunes *Phys. Rev. E* **66** 031302
- [11] Hunt J C R, Leibovich S and Richards K J 1988 Turbulent shear flows over low hills *Q. J. R. Meteorol. Soc.* **114** 1435–70
- [12] Weng W S, Hunt J C R, Carruthers D J, Warren A, Wiggs C F S, Livingstone I and Castro I 1991 Air flow and sand transport over sand-dunes *Acta Mech. Suppl.* **2** 1–22
- [13] Sauermann G, Kroy K and Herrmann H J 2001 Continuum saltation model for sand dunes *Phys. Rev. E* **64** 031305
- [14] Schwämmle V and Herrmann H J 2003 Solitary wave behaviour of sand dunes *Nature* **426** 619
- [15] Endo N, Taniguchi K and Katsuki A 2004 Observation of the whole process of interaction between barchans by flume experiments *Geophys. Res. Lett.* **31** L12503
- [16] Endo N, Sunamura T and Takimoto H 2005 Barchan ripples under unidirectional water flows in the laboratory: formation and planar morphology *Earth Surf. Process. Landforms* **30** 1675–82
- [17] Hersen P, Douady S and Andreotti B 2002 Relevant length scale of barchan dunes *Phys. Rev. Lett.* **89** 264301
- [18] Hersen P 2005 Flow effects on the morphology and dynamics of aeolian and subaqueous barchan dunes *J. Geophys. Res., Earth Surf.* **110** F04S07

- [19] Sauermann G, Rognon P, Poliakov A and Herrmann H J 2000 The shape of the barchan dunes of Southern Morocco *Geomorphology* **36** 47–62
- [20] Elbelrhiti H, Andreotti B and Claudin P 2005 Field evidence for surface-wave-induced instability of sand dunes *Nature* **437** 720–3
- [21] Elbelrhiti H, Andreotti B and Claudin P 2008 Barchan dune corridors: field characterization and investigation of control parameters *J. Geophys. Res.* **113** F02S15
- [22] Parteli E J R, Durán O and Herrmann H J 2007 Minimal size of a barchan dune *Phys. Rev. E* **75** 011301
- [23] Parteli E J R and Herrmann H J 2007 Saltation transport on Mars *Phys. Rev. Lett.* **98** 198001
- [24] Groh C, Wierschem A, Aksel N, Rehberg I and Kruehle C A 2008 Barchan dunes in two dimensions: experimental tests for minimal models *Phys. Rev. E* **78** 021304
- [25] Groh C, Wierschem A, Aksel N, Rehberg I and Kruehle C A 2009 Erratum: Barchan dunes in two dimensions: Experimental tests for minimal models [Phys. Rev. E, **78** 021304 (2008)] *Phys. Rev. E* **79** 019903
- [26] Groh C, Aksel N, Rehberg I and Kruehle C A 2009 Grain size dependence of barchan dune dynamics *AIP Conf. Proc.* **1145** 955–8
- [27] Kroy K, Fischer S and Obermayer B 2005 The shape of barchan dunes *J. Phys.: Condens. Matter* **17** S1229
- [28] Fischer S, Cates M E and Kroy K 2008 Dynamic scaling of desert dunes *Phys. Rev. E* **77** 031302
- [29] Groh C, Rehberg I and Kruehle C A 2009 How attractive is a barchan dune? *New J. Phys.* **11** 023014
- [30] Andreotti B 2004 A two-species model of aeolian sand transport *J. Fluid. Mech.* **510** 47–70
- [31] Ungar J E and Haff P K 1987 Steady state saltation in air *Sedimentology* **34** 289–99
- [32] Dong Z, Liu X, Wang H, Zhao A and Wang X 2002 The flux profile of a blowing sand cloud: a wind tunnel investigation *Geomorphology* **49** 219–30
- [33] Ni J R, Li Z S and Mendoza C 2002 Vertical profiles of aeolian sand mass flux *Geomorphology* **49** 205–18
- [34] Zhou Y-H, Guo X and Zheng X J 2002 Experimental measurements of wind-sand flux and sand transport for naturally mixed sands *Phys. Rev. E* **66** 021305
- [35] Nishimura K and Hunt J C R 2009 Saltation and incipient motion above a flat particle bed below a turbulent boundary layer *J. Fluid Mech.* **417** 77–102
- [36] Yang P, Dong Z, Qian G, Luo W and Wang H 2007 Height profile of the mean velocity of an aeolian saltating cloud: wind tunnel measurements by particle image velocimetry *Geomorphology* **89** 320–34
- [37] Creyssels M, Dupont P, Ould el Moctar A, Valance A, Cantat I, Jenkins J T, Pasini J M and Rasmussen K R 2009 Saltating particles in a turbulent boundary layer: experiment and theory *J. Fluid. Mech.* **625** 47–74
- [38] Bagnold R A 1973 The nature of saltation and of ‘bed-load’ transport in water *Proc. R. Soc. A* **332** 472–504
- [39] Collinson J D and Thompson D B 1989 *Sedimentary Structures* (Oxford: The University Printing House)
- [40] Simons D and Şentürk F 1992 *Sediment Transport Technology* (Littleton, CO: Water Resources Publications)
- [41] Osanloo F, Kolahchi M R, McNamara S and Herrmann H J 2008 Sediment transport in the saltating regime *Phys. Rev. E* **78** 011301
- [42] Anecy C, Bigillon F, Frey P, Lanier J and Ducret R 2002 Saltating motion of a bead in a rapid water stream *Phys. Rev. E* **66** 036306
- [43] Anecy C, Bigillon F, Frey P and Ducret R 2003 Rolling motion of a bead in a rapid water stream *Phys. Rev. E* **67** 011303
- [44] Charru F, Mouilleron H and Eiff O 2004 Erosion and deposition of particles on a bed sheared by a viscous flow *J. Fluid Mech.* **519** 55–80
- [45] Lobkovsky A E, Orpe A V, Molloy R, Kudrolli A and Rothman D H 2008 Erosion of a granular bed driven by a laminar fluid flow *J. Fluid Mech.* **605** 47–58
- [46] Charru F, Mouilleron H and Eiff O 2009 Inside the moving layer of a sheared granular bed *J. Fluid Mech.* **628** 229–39
- [47] Rousseaux G, Caps H and Westfreid J-E 2004 Granular size segregation in underwater sand ripples *Eur. Phys. J. E* **13** 213–9
- [48] Wang Z-T and Zheng X-J 2004 Theoretical prediction of creep flux in aeolian sand transport *Powder Technol.* **139** 123–8

- [49] Hele-Shaw H S 1898 Investigation of the nature of surface resistance of water and of stream-line motion under certain experimental conditions *Trans. Inst. Naval Arch.* **40** 21–46
- [50] Duda R O and Hart P E 1972 Use of the Hough transformation to detect lines and curves in pictures *Commun. ACM* **15** 11–5
- [51] Kimme C, Ballard D and Sklansky J 1975 Finding circles by an array of accumulators *Commun. ACM* **18** 120–2
- [52] Use of qvoronoi algorithm to calculate the Voronoi diagram, <http://www.qhull.org>
- [53] Ayrton H 1910 The origin and growth of ripple-mark *Proc. R. Soc. A* **84** 285
- [54] Oertel H Jr, Böhle M and Dohrmann U 2009 *Strömungsmechanik* (Wiesbaden: Vieweg+Teubner)
- [55] Sauer mann G, Andrade J S Jr, Maia L P, Costa U M S, Araújo A D and Herrmann H J 2003 Wind velocity and sand transport on a barchan dune *Geomorphology* **54** 245–55